Annales
Geophysicae

Role of eddy diffusion in the delayed ionospheric response to solar flux changes

Rajesh Vaishnav[1], Christoph Jacobi[1], Jens Berdermann[2], Mihail Codrescu[3], and Erik Schmölter[2]

[1]Leipzig Institute for Meteorology, Universität Leipzig, Stephanstr. 3, 04103 Leipzig, Germany
[2]German Aerospace Center, Kalkhorstweg 53, 17235 Neustrelitz, Germany
[3]Space Weather Prediction Centre, National Oceanic and Atmospheric Administration, Boulder, Colorado, USA

Correspondence: Rajesh Vaishnav (rajesh_ishwardas.vaishnav@uni-leipzig.de)

Abstract. Simulations of the ionospheric response to solar flux changes driven by the 27 d solar rotation have been performed using the global 3-D Coupled Thermosphere Ionosphere Plasmasphere electrodynamics (CTIPe) physics-based numerical model. Using the F10.7 index as a proxy for solar extreme ultraviolet (EUV) variations in the model, the ionospheric delay at the solar rotation period is well reproduced and amounts to about 1 d, which is consistent with satellite and in situ measurements. From mechanistic CTIPe studies with reduced and increased eddy diffusion, we conclude that the eddy diffusion is an important factor that influences the delay of the ionospheric total electron content (TEC). We observed that the peak response time of the atomic oxygen to molecular nitrogen ratio to the solar EUV flux changes quickly during the increased eddy diffusion compared with weaker eddy diffusion. These results suggest that an increase in the eddy diffusion leads to faster transport processes and an increased loss rate, resulting in a decrease in the ionospheric time delay. Furthermore, we found that an increase in solar activity leads to an enhanced ionospheric delay. At low latitudes, the influence of solar activity is stronger because EUV radiation drives ionization processes that lead to compositional changes. Therefore, the combined effect of eddy diffusion and solar activity leads to a longer delay in the low-latitude and midlatitude region.

1 Introduction

The solar activity plays a significant role in controlling the variations in the thermosphere–ionosphere (T/I) system, in particular through solar extreme ultraviolet (EUV) and ultraviolet (UV) radiation and their variability. In addition, there are several factors which control the behavior of the T/I system, such as tidal and gravity wave forcing from the lower atmosphere, neutral winds, and related currents in the ionosphere. These are especially predominant during low solar activity, leading to reduced correlation of solar flux and ionospheric electron density then (Vaishnav et al., 2019). The ionosphere itself is created through photoionization of the major constituents (atomic oxygen, molecular nitrogen, and molecular oxygen), while photodissociation may change the mixing ratios of these constituents (especially atomic oxygen), leading to modifications of the ionization rates.

Due to these varying ionization rates for different atoms and molecules, a series of layers of electron density forms, known as D, E, F1, and F2 regions. The maximum peak of electron density is observed in the F2 region. The F2 region electron densities mainly depend on photochemical processes, such as photodissociation, photoionization, and loss by recombination with molecular nitrogen, and transport processes, such as neutral wind and diffusion. On top of this, there are many processes which can drive or disturb the ionospheric ion distribution, such as diffusion, transport, cooling, and heating mechanisms. Transport can be divided into three main categories, namely eddy diffusion, molecular diffusion, and advection processes (Brasseur and Solomon, 2005). The

F2 region is strongly influenced by the global thermospheric circulation (Rishbeth, 1998).

The physical mechanism of the delayed ionospheric response cannot be explained with solar variations, seasonal variations, or changes due to geomagnetic activity. We also cannot explain the delay with photoionization and photodissociation processes alone. This has been discussed in several studies (Jakowski et al., 1991; Schmölter et al., 2018, 2020, and references therein), and the importance of the T/I coupling was pointed out. The T/I coupling is important for the delay. This has been mentioned in several studies by now but has scarcely been investigated. The most important impacts we would expect due to this coupling are compositional changes that can impact the major processes, and this could be due to gravity-wave-induced diffusion.

The lower thermospheric composition is not only influenced by gravity waves, but also by other parts of the lower atmospheric wave spectrum, including atmospheric tides and planetary waves. The main source of eddy diffusion is breaking of gravity waves. Gravity waves are usually generated in the lower atmosphere by various mechanisms such as convection, wind shears, storms, and airflow over mountains. Their amplification and wave breaking due to instabilities produces mixing (Li et al., 2005). Atmospheric tidal and planetary wave activity can also significantly contribute to eddy diffusion. For example, the tides induce a net transport of atomic oxygen via the mean meridional circulation generated by tidal dissipation (Jones et al., 2014a, b). Above the mesopause, the intradiurnal variability associated with atmospheric tides strongly affects the transport of NO_x (Meraner and Schmidt, 2016), and seasonally varying gravity wave and tidal mixing influence the mesosphere–lower thermosphere (MLT) region (Qian et al., 2013). Moreover, the possible role in the semiannual oscillation in thermospheric mass density is discussed by Jones et al. (2018). Siskind et al. (2014) showed that the vertical transport by nonmigrating tides causes a significant reduction in the calculated peak electron density of the ionospheric F2 layer.

Several studies have reported the influence of gravity waves and turbulence on the T/I composition and calculated the eddy diffusion coefficient in the MLT region (Kirchhoff and Clemesha, 1983; Sasi and Vijayan, 2001; Swenson et al., 2019). Based on radar measurements, Kirchhoff and Clemesha (1983) calculated a minimum (maximum) eddy diffusion coefficient of 45 (123) $m^2 s^{-1}$ during fall (summer). Similarly, Sasi and Vijayan (2001) used Doppler radar observations and show that the eddy diffusion varies from 25 to 300 $m^2 s^{-1}$ during September and June.

Turbulent mixing is an important process affecting the composition of the T/I system. The effect of turbulence on different minor and major species has been discussed on several occasions (e.g., Keneshea and Zimmerman, 1970; Shimazaki, 1971; Chandra and Sinha, 1974; Rishbeth et al., 1987; Rees and Fuller-Rowell, 1988; Fuller-Rowell and Rees, 1992; Danilov and Konstantinova, 2014; Pilinski and

Crowley, 2015; Swenson et al., 2018). Various coupled models have been developed to understand the T/I region variations, considering the availability of experimental and theoretical knowledge. Earlier 1-D models, which include eddy diffusion coefficients, have been used to model the T/I region (e.g., Colegrove et al., 1965; Shimazaki, 1971; Jakowski et al., 1991). Nowadays, more improved, 3-D models like the Coupled Thermosphere Ionosphere Plasmasphere Electrodynamics (CTIPe) model (Fuller-Rowell and Rees, 1980) or the National Center for Atmospheric Research (NCAR) Thermosphere–Ionosphere–Electrodynamics General Circulation Model (TIE-GCM) (Richmond et al., 1992) are available to explore the dynamics of the T/I region. These models cannot be expected to reproduce the real ionospheric variability exactly due to limited knowledge of various processes in the T/I region and their corresponding inputs (e.g., Shim et al., 2011; Codrescu et al., 2012), but they are capable of providing insight into relevant dynamical processes in the T/I.

Rees and Fuller-Rowell (1988) used a sinusoidal eddy turbulence profile and analyzed the effect of eddy turbulence on temperature, atomic oxygen, and nitric oxide. They showed that an increase in turbulence near the mesopause leads to an increase in atomic oxygen and nitric oxide. This leads to a change in the thermal structure by strongly modifying the gravity wave flux.

The solar radiation reaching the Earth exhibits a periodicity of about 27 d, owing to the solar rotation. As a result, the T/I system also varies with this periodicity. Many studies revealed a delay in ionospheric parameters, such as total electron content (TEC, given in TEC units, 1 TECU = 10^{16} electrons m^{-2}), electron density, peak electron density of F_2 region (NmF2, cm^{-3}), and the corresponding height (hmF2, km), to the 27 d solar flux variation (Jakowski et al., 1991; Liu et al., 2006; Afraimovich et al., 2008; Lee et al., 2012; Anderson and Hawkins, 2016; Jacobi et al., 2016; Schmölter et al., 2018, 2020, 2021; Vaishnav et al., 2018, 2021; Ren et al., 2018, and references therein). Most of the studies found an ionospheric delay of about 1–2 d, with a possible uncertainty of about half a day. Schmölter et al. (2018), using high temporal resolution data, found an ionospheric delay of about 17–19 h using TEC and Geostationary Operational Environmental Satellite (GOES) EUV datasets. The detailed seasonal and spatial effect on the ionospheric delay was studied by Schmölter et al. (2020). Their study revealed a strong geomagnetic effect on the ionospheric delay. They also noticed that the delay over Southern Hemisphere stations is larger than over Northern Hemisphere stations.

Numerical simulations using a 1-D model have revealed that the delay might be due to the slow diffusion of atomic oxygen at 180 km height, generated by solar UV radiation in the Schumann–Runge continuum, causing photodissociation of molecular oxygen above the turbopause (Jakowski et al., 1991).

Ren et al. (2018) investigated the ionospheric time delay using observations and simulations with the TIE-GCM model. They discussed the possible role of ion production and loss mechanisms and the O/N_2 ratio in the ionospheric delay against the solar EUV flux. A strong effect of geomagnetic activity was reported. The ionospheric response time is controlled by photochemical, dynamical, and electrodynamical processes. Ren et al. (2019) suggested that the time delay in thermospheric temperature is due to the difference between the total heating and cooling rates. The study also found a possible role of the general circulations in the upper atmosphere in the time delay. Similarly, the peak response time of the neutral mass density corresponds to the time of equilibrium between the effect of the barometric process and the change in its abundance (Ren et al., 2020). Moreover, Ren et al. (2021) suggest the possible role of geomagnetic activity in the time delay of the thermospheric mass density, which varies with altitude, latitude, and local time.

Despite such a general understanding, however, the exact mechanism of the ionospheric delay needs further investigation. Therefore, here we attempt to quantify the process which is probably responsible for the ionospheric delay using the CTIPe model (Fuller-Rowell and Rees, 1980). Vaishnav et al. (2018) indicated that transport processes might play an important role in the ionospheric delay observed in TEC using CTIPe model simulations. Based on this assumption, numerical simulations have been performed to consolidate the preliminary results of Vaishnav et al. (2018) and the hypothesis of Jakowski et al. (1991) and to explain the physical mechanisms of the ionospheric delay. To understand the role of T/I coupling in this study, we perform model runs changing the eddy diffusion.

An ionospheric delayed response has been investigated by Schmölter et al. (2020) over European stations. They reported an ionospheric delay of about 18 h over these stations. Therefore, in this paper, the emphasis is to reproduce and investigate the ionospheric delay response over a European location (40° N).

2 CTIPe model simulations

The CTIPe model is used to understand the influence of eddy diffusion in the neutral composition and its role in the delay mechanism. The CTIPe model is an advanced version of the CTIM model (Fuller-Rowell et al., 1987) and is a global, first-principle, nonlinear, time-dependent, 3-D, numerical, physics-based coupled thermosphere–ionosphere–plasmasphere model consisting of four fully coupled distinct components, namely, (a) a neutral thermosphere model (Fuller-Rowell and Rees, 1980); (b) a high-latitude ionosphere convection model (Quegan et al., 1982); (c) a midlatitude and low-latitude ionosphere plasmasphere model (Millward et al., 1996); and (d) an electrodynamics model (Richmond et al., 1992). The thermosphere component of the

CTIPe model solves the continuity, momentum, and energy equations to calculate the wind components, global temperature, and composition.

The transport terms particularly specify the $E \times B$ drift and include ion-neutral interactions under the effect of the magnetospheric electric field. The geographic latitude/longitude resolution is $2°/18°$. In the vertical direction, the atmosphere is divided into 15 logarithmic pressure levels at an interval of one scale height, starting with a lower boundary at 1 Pa (about 80 km altitude) to above 500 km altitude at pressure level 15. The high-latitude ionosphere (poleward of geomagnetic coordinates 55° N/S) and the midlatitude and low-latitude ionosphere and plasmasphere are implemented as separate components, and there is an artificial boundary between these two model components. The equations for the neutral thermosphere model are solved self-consistently with a high-latitude ionosphere model (Quegan et al., 1982). The numerical solution of the composition equation describes transport, turbulence, and diffusion of atomic oxygen, molecular oxygen, and nitrogen (Fuller-Rowell and Rees, 1983). External inputs are needed to run the model, such as solar UV and EUV, Weimer electric field, TIROS/NOAA auroral precipitation (note, however, that particle precipitation is turned off during our simulations), and tidal forcing from the Whole Atmosphere Model (WAM). The F10.7 index (Tapping, 1987) is used as a solar proxy for calculating ionization, heating, and oxygen dissociation processes. Within CTIPe, a reference solar spectrum based on the EUVAC model (Richards et al., 1994) and the Woods and Rottman (2002) model, driven by variations of F10.7 input, is used. The EUVAC model is used for the wavelength range from 5 to 105 nm and the Woods and Rottman (2002) model from 105 to 175 nm. Solar flux is obtained from the reference spectra using the following equation:

$$f(\lambda) = f_{\mathrm{ref}}(\lambda)[1 + A(\lambda)(P - 80)], \tag{1}$$

where f_{ref} and A are the reference spectrum and a solar variability factor, and $P = 0.5 \times (\mathrm{F10.7} + \mathrm{F10.7}A)$, where F10.7A is the average of F10.7 over 41 d. Detailed information on the CTIPe model is available in Codrescu et al. (2008, 2012).

In this paper, our primary goal is to understand the influence of eddy diffusion on the ionospheric response during the 27 d solar rotation. Therefore, several model runs were performed in this study with different diffusion conditions under different artificial solar activity conditions. Three runs were performed with sinusoidally varying solar activity from 75–125 sfu, keeping all other conditions constant. Constant atmospheric and astronomical conditions of 15 March 2013 were used to perform these experiments.

Several authors have suggested that the eddy diffusion is strongly varying based on the months or seasons (e.g., Kirchhoff and Clemesha, 1983; Sasi and Vijayan, 2001; Swenson et al., 2019). Therefore, the experiments were performed using an eddy diffusion coefficient K_T, which amounts to 75 %,

100 %, and 125 % of the original values in the model, and we refer to these runs as $K_T \times 0.75$, $K_T \times 1.0$, and $K_T \times 1.25$, where $K_T \times 1.0$ represents the reference run.

3 Mechanistic studies

In the CTIPe model, the T/I composition is calculated by combining the continuity equation with the diffusion equation. The model estimates changes in the composition of the major species (O, O_2, and N_2) self-consistently, including wind and temperature (Fuller-Rowell and Rees, 1983), as well as molecular diffusion, production, and loss mechanisms.

The continuity equation for the mass mixing ratio, $\psi_i = (n_i \cdot m_i)/\rho$ of the ith species, with n_i as number density, m_i as the molecular mass, and ρ as atmospheric density, may be written as

$$\frac{\partial \psi_i}{\partial t} = \frac{1}{\rho}(m_i S_i) - \boldsymbol{V} \cdot \nabla \psi_i - \omega \frac{\partial \psi_i}{\partial p}$$
$$- \frac{1}{\rho} \nabla \cdot (n_i m_i \boldsymbol{C}_i) + \frac{1}{\rho} \nabla \cdot (K_T n \nabla m \psi_i), \quad (2)$$

where S_i represents sources and sinks of the species, K_T is the eddy diffusion coefficient, $\boldsymbol{V}$ is the horizontal neutral wind vector, n is the total number density, m is the mean molecular mass, and $\boldsymbol{C}_i$ is the diffusion velocity of the ith species. The terms on the right-hand side of Eq. (2) are, in their respective order, sources and sinks of species, horizontal advection, vertical advection, molecular diffusion, and eddy diffusion.

The mathematical form of the eddy diffusion coefficient K_T used in the CTIPe model as a function of height is given by Shimazaki (1971) and Fuller-Rowell and Rees (1992):

$$K_T = D \exp\left(-A_1(h - h_o)^2\right) \quad h \geq h_o, \quad (3)$$

$$K_T = (D - D_o)\exp\left(-A_2(h - h_o)^2\right)$$
$$+ D_o \exp\left(-A_3(h - h_o)\right) \quad h \leq h_o. \quad (4)$$

A peak value of $D = 150\,\text{m}^2\,\text{s}^{-1}$ at $h_o = 105\,\text{km}$ altitude and $D_o = 100\,\text{m}^2\,\text{s}^{-1}$ is used for the $K_T \times 1.0$ reference run. The shape parameters $A_1 = 0.03$, $A_2 = 0.03$, and $A_3 = 0.05$ are taken from Shimazaki (1971). As pointed out by Fuller-Rowell and Rees (1992), eddy diffusion has the greatest influence on atomic oxygen and nitric oxide in the lower thermosphere. A detailed description of the chemistry of the major species is available in Fuller-Rowell (1984).

In our experiments, the CTIPe model was first run with constant F10.7 input for 10 d to achieve a diurnally reproducible condition, and after this spin-up, F10.7 was modified for 27 d using a sine function:

$$\text{F10.7}(t) = 100 - 25\cos\left(\frac{2\pi t}{27}\right), \quad (5)$$

where t represents the time in days.

The various terms of the composition equation are shown in Fig. 1 for the noontime (12:00 UT) for the atomic oxygen mass mixing ratio (ψ_O) at 40° N, 18° E in the reference run. The figure shows the behavior of all terms at pressure level 12 (260 km). The vertical dashed red line shows the maximum of the input solar flux as per Eq. (2). Figure 1a shows that the molecular diffusion term shows a delay of less than 1 d for ψ_O. The horizontal and vertical advection are decreasing with the increasing input solar flux with a delay of less than 1 d and 1 d, respectively (Fig. 1b). Similar variations can be seen in the chemical production and loss terms (source and sink term). The delay between production and loss is about 1–2 d in the case of ψ_O, as shown in Fig. 1c. The change in the production term in the composition equation is based on the photoionization processes contributing to ψ_O.

Ren et al. (2020) discussed the physics behind the time delay in different thermospheric neutrals. They found that the peak response time of the mass density of the neutrals (O and N_2) corresponds to the time of equilibrium between the effect of the barometric process and the change in their abundance.

Figure 2 shows the daily zonal mean TEC for three different runs with different eddy diffusion coefficients as a function of time and magnetic latitude. The zonal averages represent the average TEC values over all longitudes at a specific magnetic latitude. In the CTIPe model, TEC is calculated over the altitude range from 80 to 2000 km. In Fig. 2, the zonal mean TEC is shown by the contours, and the white curves show the corresponding variability of the F10.7 index. Here, moderate solar activity conditions (75–125 sfu) have been used.

The daily zonal mean TEC show the overall effect of solar flux on the T/I system, since we used constant atmospheric and astronomical conditions for these simulations.

The results from the reference run $K_T \times 1.0$, with the original value of the eddy diffusion coefficient, are shown in Fig. 2b. The simulations reproduce the real latitudinal as well as temporal variations with the variability in the solar flux. The zonal mean TEC distributions are symmetric around the geomagnetic equator, with maximum amplitudes of about 70 TECU. The TEC values decrease towards the high latitudes. The distribution of TEC highly depends on the ionization of neutrals and various processes such as transport and recombination. The TEC amplitude variations reflect the effects of solar activity and compositional changes.

The $K_T \times 0.75$ run results are shown in Fig. 2a. It shows an increase of TEC in the low-latitude to midlatitude region in comparison to the reference run. The reduction of turbulence leads to slower transport and an increase in TEC. Figure 2c shows the zonal mean TEC for the $K_T \times 1.25$ run. In comparison to the reference run, TEC is reduced by a significant amount. These results show that eddy diffusion has a direct impact on TEC.

Figure 3a shows the global mean TEC (GTEC) as simulated by the three different runs along with the F10.7 in-
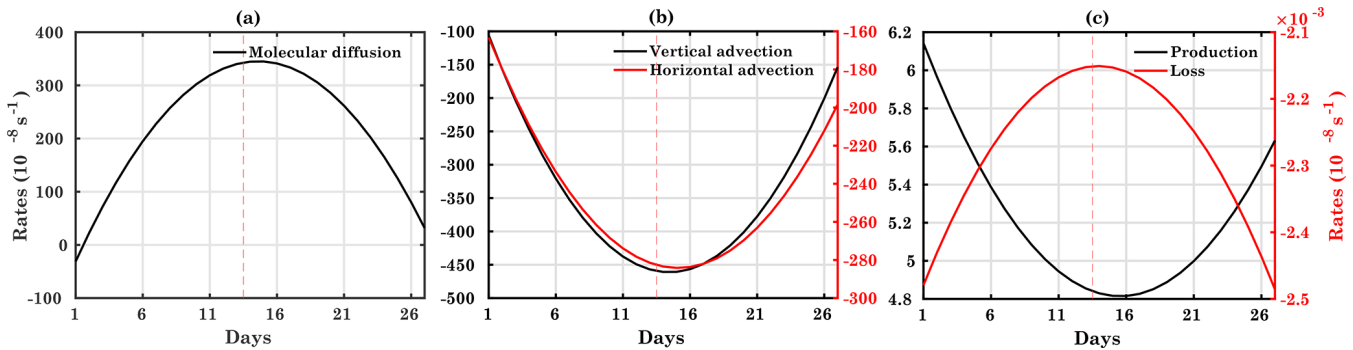
Figure 1. Time series of different terms: **(a)** molecular diffusion, **(b)** horizontal advection and vertical advection, and **(c)** production and loss for atomic oxygen mass mixing ratio. Both the y axes are marked with the corresponding color. The vertical dashed red line represents the middle of the 13th model day. All the parameters are plotted for pressure level 12 (260 km) for noontime at 40° N, 18° E.
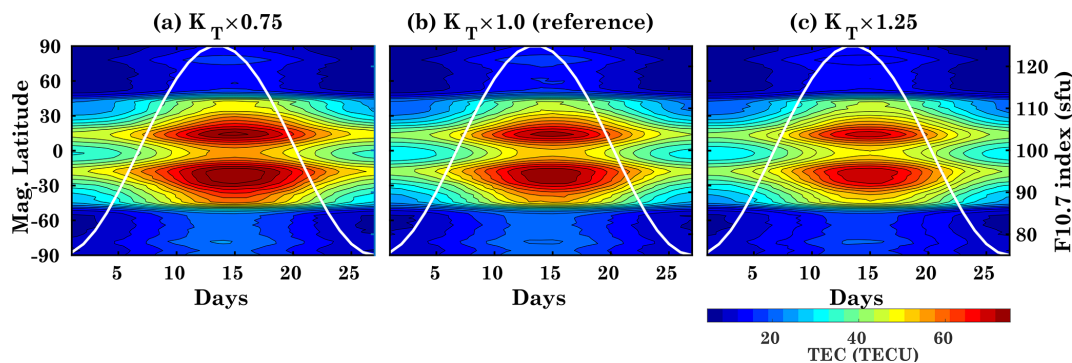

Figure 2. CTIPe-simulated daily mean zonal mean TEC for the runs **(a)** $K_T \times 0.75$, **(b)** $K_T \times 1.0$ (reference), and **(c)** $K_T \times 1.25$. The white curves show the F10.7 index input.

dex (white curve). It shows an obvious 27 d variation of GTEC corresponding to the F10.7 index variations but with a slightly different delay for the different runs. The GTEC values vary from about 8 TECU to maximum values of about 15 TECU for the reference run, corresponding to the solar flux variation. It can be seen that TEC increases linearly with F10.7. In comparison to the reference run, TEC values decreased significantly for the increased eddy diffusion condition, while it is increased for the reduced eddy diffusion conditions (see also Fig. 2).

The model F10.7 index input has been calculated according to Eq. (5) but as hourly values in order to calculate the delay and cross-correlation between GTEC and F10.7, which are shown in Fig. 3b.

For the reference run $K_T \times 1.0$, the delay is about 24 h, which is close to the value derived from observations as reported by Schmölter et al. (2018, 2020). Therefore, the model is capable of reproducing the observed ionospheric delay. In the case of reduced eddy diffusion to 75 % of the original value in run $K_T \times 0.75$, the delay is somewhat longer (about 25 h). This indicates that the delay increases due to the slower transport processes in this run. In line with this, with increased transport in the $K_T \times 1.25$ run, the delay reduces

to 20 h. These results suggest that an increase in the eddy diffusion leads to faster transport processes and an increased loss rate, resulting in a decrease of the ionospheric time delay. The loss rates are discussed below. The ionospheric time delay is mainly due to the imbalance between the production and loss of the ions and electrons (Ren et al., 2018).

We also analyzed the model results separately for the Northern Hemisphere (NH) and the Southern Hemisphere (SH), but the differences between the hemispheres are small and amount to 3, 4, and 4 h for the $K_T \times 0.75$, $K_T \times 1.0$, and $K_T \times 1.25$ runs, respectively (not shown).

Figure 4 shows the variation of the time delay at low [$\pm 30°$], middle [$\pm (30–60°)$], and high [$\pm (60–90°)$] geomagnetic latitudes for different eddy diffusion conditions. At low latitudes (Fig. 4a), the delay is more sensitive to eddy diffusion than at middle and high latitudes, as this region is not only controlled by the EUV. Here, dynamics plays an essential role, especially in the equatorial ionization anomaly. Thus, small changes in eddy diffusion can lead to a more significant change in the ionospheric delay. In general, the delay at low latitudes is longer than for the global average in Fig. 3. For the $K_T \times 1.25$ run, the delay is reduced by 4 h compared to the reference run.
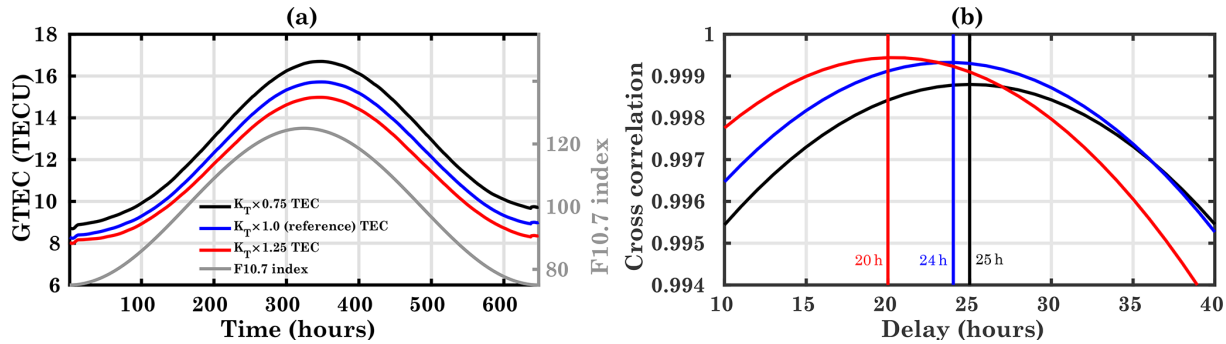
Figure 3. **(a)** Time series of modeled GTEC for different runs **(a)** $K_T \times 0.75$, **(b)** $K_T \times 1.0$ (reference), and **(c)** $K_T \times 1.25$, together with F10.7 given as a gray line. **(b)** Cross-correlation and the delay between global mean TEC and F10.7 for the different runs.
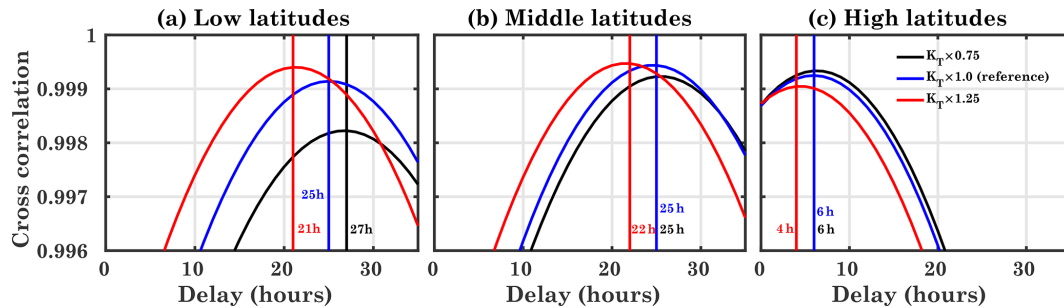

Figure 4. Cross-correlation and the delay between regional mean TEC and the F10.7 index at low **(a)**, middle **(b)**, and high **(c)** geomagnetic latitudes for different runs.

At midlatitudes (Fig. 4b) the delay in the $K_T \times 1.25$ run is about 22 h; i.e., it is longer than on a global average. This is also true for the other runs where the delay is qualitatively the same and amounts to about 25 h. In this region for run $K_T \times 0.75$, the delay is similar to the one of the reference run and is about 25 h.

At high latitudes (Fig. 4c), the variation in the delay is qualitatively the same as at middle and low latitudes; i.e., a decrease in diffusion increases the delay and vice versa. However, at high latitudes, a change in diffusion has a smaller effect, and the delay varies between 4 and 6 h for the different runs. For all runs, the delay is much smaller at high latitudes than at midlatitudes. In comparison to low-latitudes and midlatitudes, the high latitudes show less time delay in run $K_T \times 0.75$. The delay in high latitudes is also less sensitive to diffusion changes compared to the low-latitude and midlatitude regions. Similar to the runs presented in Fig. 3, the model has been run for low solar activity conditions with F10.7 in the range 70–90 sfu and using four different diffusion conditions, $K_T \times 0.5$, $K_T \times 1.0$ (reference), $K_T \times 1.5$, and $K_T \times 2.0$, which amounts to 50 %, 100 %, 125 %, and 150 % of the original values in the model, respectively, as shown in Fig. 5. Figure 5a shows the time series of TEC for different runs and the F10.7 input. In comparison to Fig. 3a, the TEC values are smaller, following the F10.7 index. For these runs, the magnitude of eddy diffusion has

been changed by 50 %. Therefore, significant differences in TEC size are observed. In the reference run, TEC varies from about 8 TEC to 11.3 TECU, while it shows a similar pattern for decreased/increased eddy diffusion with the difference in relative amplitude of TEC. The difference in the TEC curves in Fig. 5a depends on the solar flux and the magnitude of the eddy diffusion coefficient. Also, the delay is calculated using the hourly TEC datasets and the F10.7 index, as shown in Fig. 3a. For the reference run $K_T \times 1.0$, the delay in the simulated GTEC is about 19 h, while the delay increases to 34 h for the $K_T \times 0.5$ run, and it decreases with the increased diffusion conditions. Here, the delay is more sensitive to the eddy diffusion compared to the 25 % change cases, since the solar activity is less dominant. Compared to low solar activity, the eddy diffusion is less dominant in moderate solar activity, and the delay fluctuations are smaller. It should be noted that increasing solar activity leads to an increase in ionospheric delay.

To shed more light on the spatial patterns of the correlation between the F10.7 index and TEC, as well as on the ionospheric delay, the latter is shown in Fig. 6 for each model grid point. Figure 6b shows the spatial map for the reference run $K_T \times 1.0$. Maximum longitudinal differences are observed in the low-latitude and midlatitude region. Near the equatorial region, the delay varies from 10 to 40 h. At high latitudes, the delay is about 0 to 10 h.
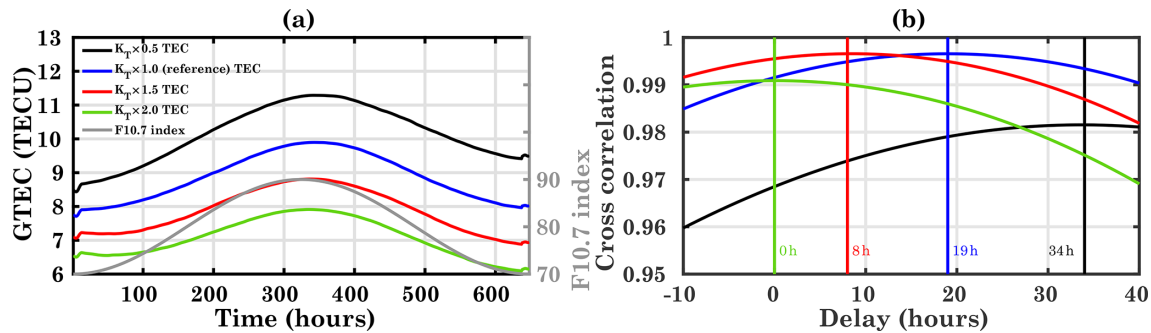
Figure 5. (a) Time series of modeled TEC for the different diffusion conditions $K_T \times 0.5$, $K_T \times 1.0$ (reference), $K_T \times 1.5$, and $K_T \times 2.0$. F10.7 is added as a gray line. **(b)** Cross-correlation and the delay between global mean TEC and F10.7 for the different diffusion conditions.
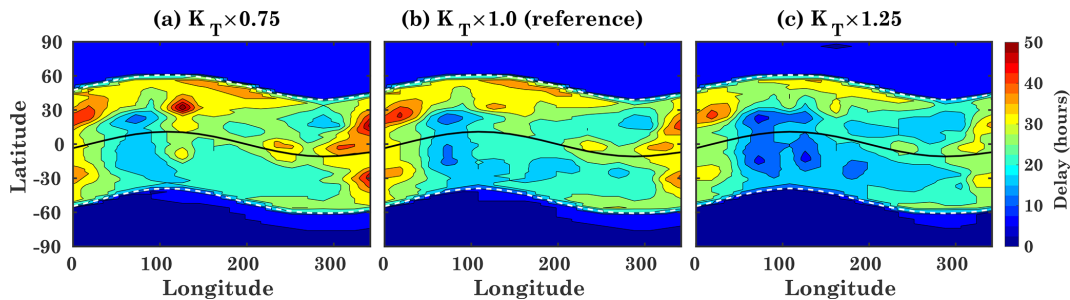

Figure 6. Spatial distribution of time delay between the CTIPe-TEC and the F10.7 index for different transport conditions, **(a)** $K_T \times 0.75$, **(b)** $K_T \times 1.0$ (reference), and **(c)** $K_T \times 1.25$. The black line represents the magnetic equator, and dashed white lines represent magnetic latitudes (55° N/S).
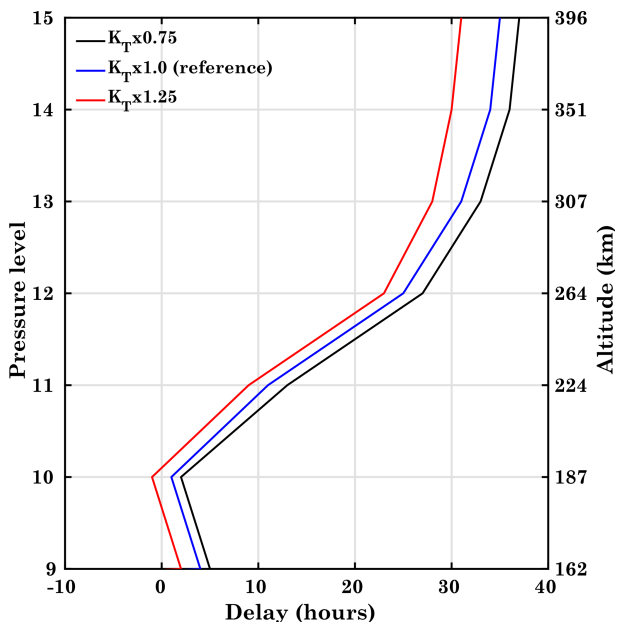
Figure 7. Vertical distribution of time delay between the atomic oxygen ion density and the F10.7 index for different transport conditions, $K_T \times 0.75$, $K_T \times 1.0$ (reference), and $K_T \times 1.25$, at geographic coordinates 40° N, 18° E.

The longitudinal variation of the delay follows the magnetic field. The maximum delay is, in line with the results in Fig. 4, generally observed at lower and middle latitudes.

As is the case with GTEC, at all latitudes, the delay in local TEC is generally increased in run $K_T \times 0.75$ and decreased in run $K_T \times 1.25$ with respect to the $K_T \times 1.0$ run. In the CTIPe model, the low-latitude and midlatitude ionosphere model and the high-latitude ionosphere model are implemented separately. Therefore, the significant change in delay seen at 55° N/S may be owing to model peculiarities in CTIPe.

In the following, we investigate the height variation of the delay using the atomic oxygen ion density at geographic coordinates 40° N, 18° E (magnetic latitude 39.06° N). Figure 7 shows the delay between the atomic oxygen ion density and the F10.7 index at different pressure levels. At pressure level 12 (260 km), the delay is about 24, 18, and 6 h for the different eddy diffusion cases $K_T \times 0.75$, $K_T \times 1.0$, and $K_T \times 1.25$, respectively. The delay continues to increase above pressure level 12, where it is quite close to the delay observed in TEC. This is owing to the fact that the delay observed in TEC is mainly determined by the delay of the F region, i.e., at higher pressure levels (200–260 km).

The eddy diffusion can influence the general circulation and hence the thermospheric neutral species. However, the thermospheric circulation is controlled not only by eddy dif-
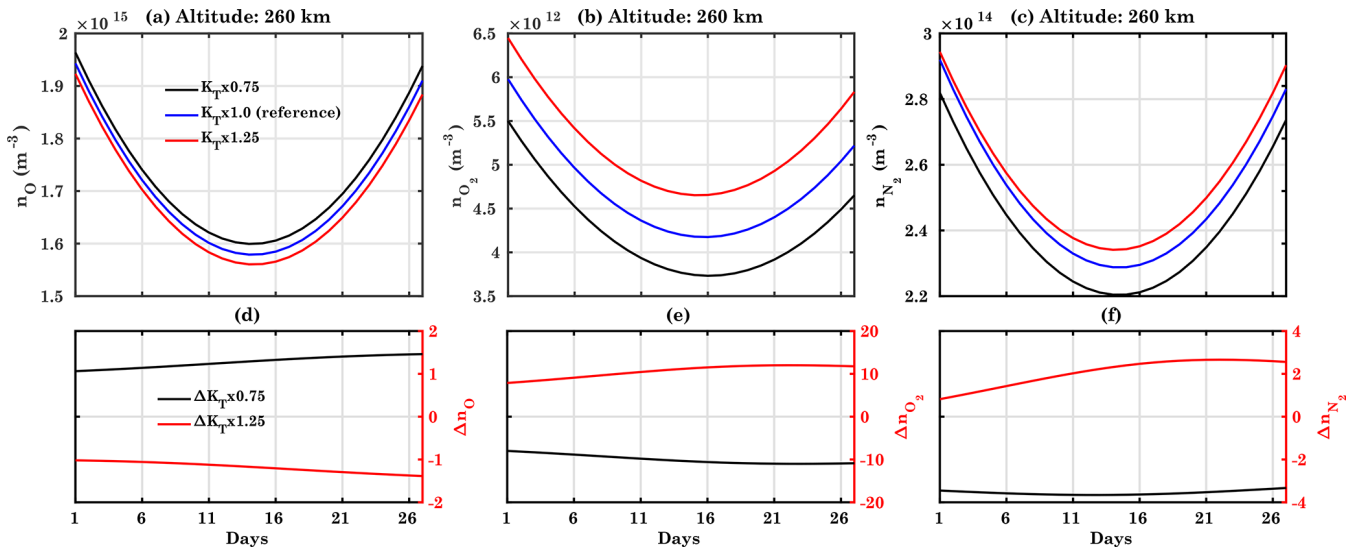
Figure 8. Variation of the CTIPe-simulated **(a)** n_O, **(b)** n_{O_2}, and **(c)** n_{N_2} for different diffusion conditions $K_T \times 0.75$ (black), $K_T \times 1.0$ (blue), and $K_T \times 1.25$ (red) (upper panel) for pressure level 12 (260 km). The percentage difference between the $K_T \times 1.0$ run (blue curve) and the runs with modified eddy diffusion conditions, $K_T \times 0.75$ (black) and $K_T \times 1.25$ (red), is shown in the lower parts of the panels.
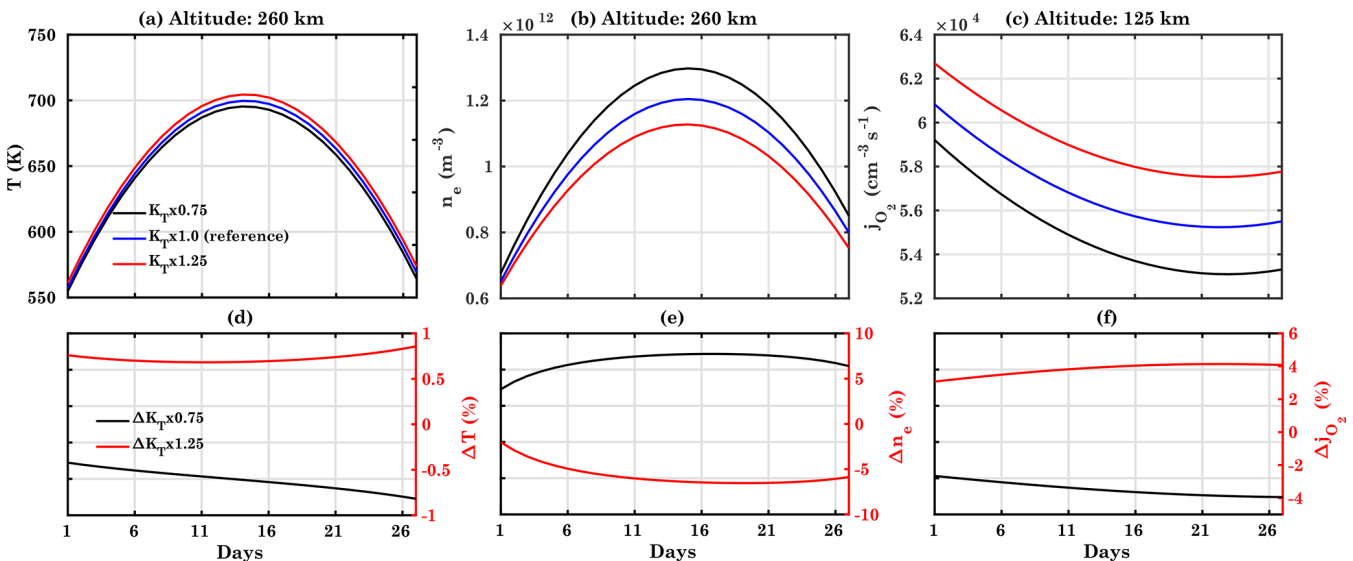

Figure 9. Same as Fig. 8 for **(a)** T, **(b)** n_e for the pressure level 12 (~ 260 km), and **(c)** j_{O_2} for pressure level 7 (~ 125 km).

fusion, but also by temperature, pressure, and neutral species, etc. All these parameters are affected by solar EUV radiation. To investigate how eddy diffusion affects the T/I system, we further analyze the evolution of various parameters such as the atomic oxygen number density (n_O), molecular oxygen density (n_{O_2}), molecular nitrogen density (n_{N_2}), molecular oxygen dissociation rates (j_{O_2}), neutral temperature (T), and electron density (n_e). Figures 8 and 9 show the variations of these parameters for the 27 d cycle for the reference run (blue color in the upper panel) and percentage differences (lower panel: on the second y axis) from the reference run

for the other diffusion conditions, $K_T \times 0.75$ and $K_T \times 1.25$, respectively, at geographic coordinates 40° N, 18° E.

Figure 8 shows the variation of n_O, n_{N_2}, and n_{O_2} at pressure level 12 (~ 260 km). Eddy diffusion has a strong influence on O, N_2, and O_2. Figure 8a shows the variations of the atomic oxygen density at pressure level 12 for a 27 d solar rotation period. It shows that the atomic oxygen density decreases with increasing solar flux, connected with an increase in temperature, which is shown in Fig. 9a. In comparison to the reference run, the percentage difference increases to about 1 % for the $K_T \times 0.75$ run during the 27 d run. This is partly, but not completely, due to the temperature decrease by
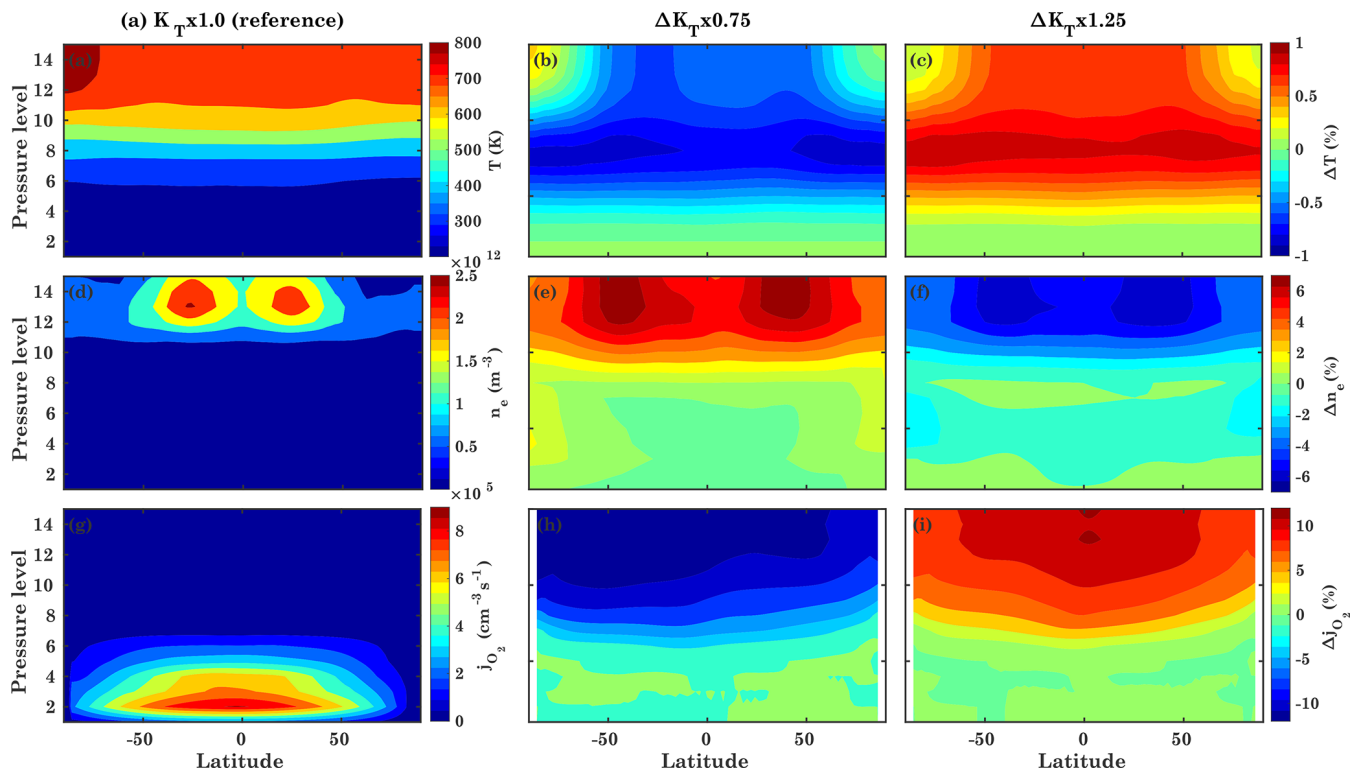
Figure 10. (a) CTIPe-simulated T (upper row), n_e (middle row), and j_{O_2} (bottom row), for the 14th model day. The other columns show the percentage difference between the $K_T \times 1.0$ simulation and the simulations with modified eddy diffusion conditions: (b) $K_T \times 0.75$ and (c) $K_T \times 1.25$.

$\sim 0.7\%$ (Fig. 9a). Thus, reduced transport leads to reduced atomic oxygen. For the $K_T \times 1.25$ run, the atomic oxygen density decreases by about 1.5 %. These differences are not connected with the solar cycle but evolve gradually over the full time interval.

Similar to the atomic oxygen density variations, the molecular oxygen and nitrogen densities also decrease with increasing solar flux (Fig. 8b and c). For the molecular oxygen density, the percentage difference decreases to about 10 % for the $K_T \times 0.75$ run, while it increases to about 10 % for the $K_T \times 1.25$ run. Similar variations are observed in the behavior of the molecular nitrogen density (Fig. 8c). Once the diffusion increased, the n_{O_2} increases compared to the reference run, demonstrating that diffusion is a critical process to control the evolution of oxygen. Therefore, we register a change in the total composition due to an increase or decrease in eddy diffusion.

Figure 8d and b show the percentage difference between the reference run results and those of the runs with increased or decreased eddy diffusion. For the $K_T \times 0.75$ run, the atomic oxygen density increases to about 1 %, while the molecular oxygen decreases by 10 %. Similar to the molecular oxygen, the molecular nitrogen density also decreases by $\sim 3\%$. In comparison to $K_T \times 0.75$, opposite trends can be seen for the $K_T \times 1.25$ run.

In Fig. 9a and b, the 27 d behavior at an altitude of ~ 260 km is shown for T and n_e. T increases with increasing solar irradiance. As an increase in solar irradiance expands the range of the thermosphere region, the scale height of each component changes. An increase in solar radiation flux will also increase the height of each pressure level. In Fig. 9e, non-monotonic variations are observed in the difference between the reference run and $K_T \times 1.25$. This could be due to the combined effect of different diffusion cases and solar flux. Compared to the reference case, the temperature decreases by about 0.7 % for the $K_T \times 0.75$ run, while it increases by 0.7 % for the $K_T \times 1.25$ run. Similar to T, n_e also varies with the solar flux. An increase in the solar radiation flux leads to an increase in ionization and thus to an increase in electron density.

The j_{O_2} also vary for different diffusion conditions, as shown in Fig. 9c for pressure level 7 (altitude ~ 125 km). An increase in eddy diffusion reduces j_{O_2}, leading to an increase in n_{O_2} and a reduction in n_O. Exactly the opposite behavior is observed for a decrease in eddy diffusion.

Since we are dealing with vertical transport processes, it is essential to analyze the latitudinal variation against pressure levels. Figure 10 shows the percentage difference of T, j_{O_2}, and n_e in the $K_T \times 0.75$ and $K_T \times 1.25$ runs with respect to $K_T \times 1.0$ for the 14th model day. Figure 10b and
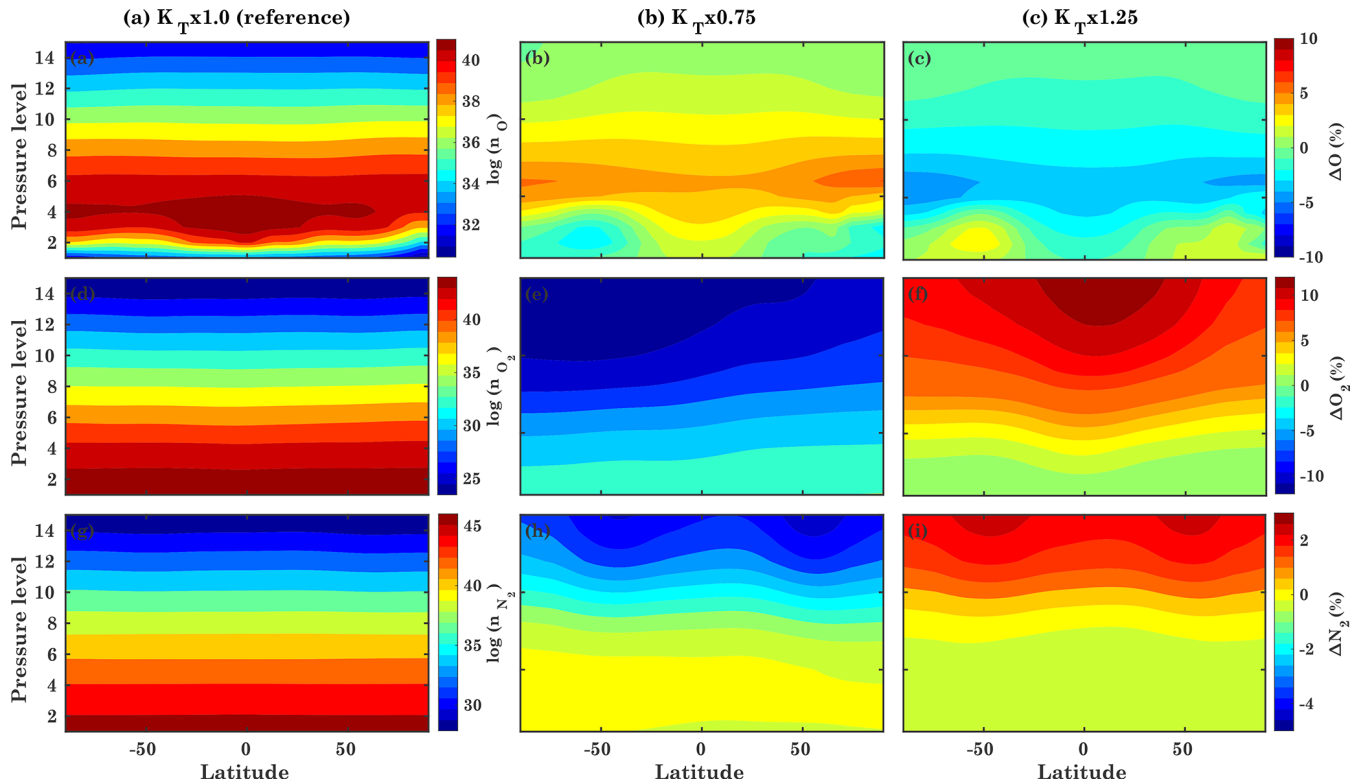
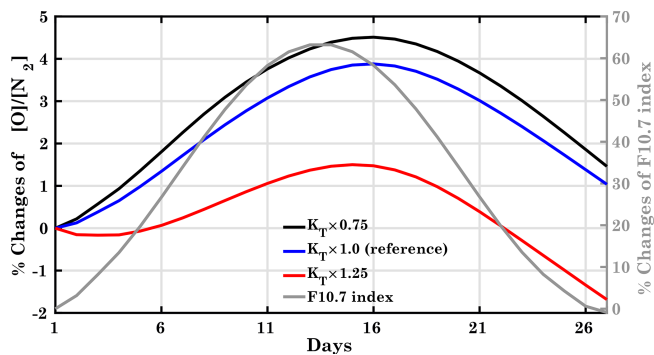**Figure 11.** Same as Fig. 10 but for n_O, n_{O_2}, and n_{N_2}.

Figure 12. Percentage change of the [O]/[N$_2$] ratio for different diffusion conditions, $K_T \times 0.75$, $K_T \times 1.0$ (reference), and $K_T \times 1.25$, at pressure level 12 at geographic coordinates 40° N, 18° E. The right y axis refers to the percentage change of the F10.7 index (gray curve).

c show that due to a decrease/increase in eddy diffusion, T decreases/increases at all pressure levels.

The lowest four pressure levels belong to the lower boundary, where the neutral wind, temperature, and height of the pressure level are imposed as boundary conditions from the WAM model. An increase of the eddy diffusion by a factor of 25 % ($K_T \times 1.25$) leads to an increase in T by 1 %. It mainly affects pressure levels 7–9 (125–160 km). The percentage

difference in T is negligible at pressure levels 5–6 (110 km), but the variations increase with altitude. Figure 10d shows the latitude–pressure distribution of n_e. For the $K_T \times 0.75$ run, it shows that for a reduction in eddy diffusion, n_e is increased in the thermosphere above pressure level 9 (160 km). Interestingly, above this altitude, n_e increases by about 7 %. Electron density increases in the low-latitude region at pressure level 4 (98 km) and in the high-latitude region at pressure level 5 (105 km). The response of the thermosphere n_e to an enhancement of eddy diffusion is entirely different. For the $K_T \times 1.25$ run, n_e decreases at higher pressure levels, but it increases at lower pressure levels, except for midlatitudes at 98 km and high latitudes at 105 km.

The variation in j_{O_2} is shown in Fig. 10g. The percentage difference for the $K_T \times 0.75$ run compared to the reference run decreases by about 7% for pressure levels 5–7 (105–125 km), and it decreases by 7 % for the $K_T \times 1.25$ run.

Figure 11a shows the variation of n_O. For the $K_T \times 0.75$ run, n_O is increased by 5 %–7 % above the turbopause. The enhanced diffusion leads to an increase of n_O in the lower thermosphere due to the downward transport of n_O from higher altitudes (Rees and Fuller-Rowell, 1988). Note that eddy diffusion has a more substantial impact at high latitudes below the turbopause. Chandra and Sinha (1974) showed that due to photochemical effects, the variation of eddy diffusion
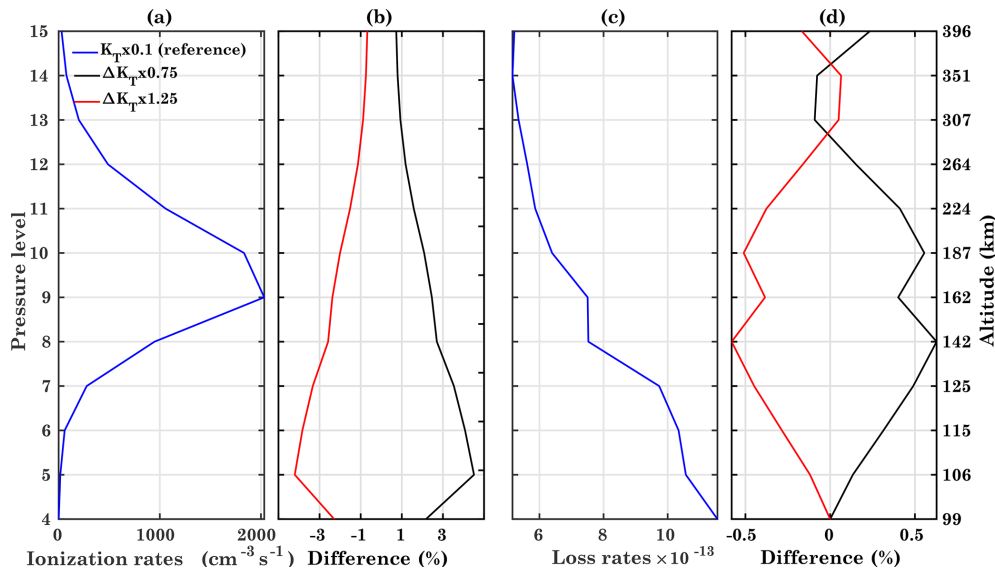
Figure 13. Atomic oxygen ionization (**a**) and loss rates (**c**) due to molecular nitrogen for the reference run $K_T \times 1.0$ and its difference (**b, d**) with $K_T \times 0.75$ and $K_T \times 1.25$ at different pressure levels on the 14th model day at geographic coordinates 40° N, 18° E.

does not contribute significantly to n_O below 100 km, but above 100 km it decreases with increasing eddy diffusion.

Enhanced eddy diffusion leads to an increase in n_{O_2} of about 10 %–12 % above the turbopause in the $K_T \times 1.25$ run, with j_{O_2} decreasing by about 0.5 %, as shown in Fig. 10d. Thus, the decrease in j_{O_2} increases n_{O_2}, and this leads to a decrease in n_O. Similar variations are also observed in the case of enhanced diffusion conditions for n_{N_2}, with an increase of about 2 %–3 % for the enhanced eddy diffusion conditions. The variation in eddy diffusion affects the composition at different altitudes through molecular diffusion.

Enhanced eddy diffusion leads to an increase in molecular oxygen. This leads to a decrease in atomic oxygen at all altitudes above 100 km due to molecular diffusion. As a result, there is a significant decrease in the [O]/[N$_2$] ratio. Qian et al. (2009) studied the effect of modified eddy diffusion on thermospheric composition using the NCAR TIE-GCM model and reported similar results. These simulations revealed a new finding how eddy diffusion can strongly affect the thermospheric composition (O, O$_2$, and N$_2$) through the ionospheric delay.

The steady-state electron density N can be written according to Rishbeth (1998):

$$N \sim \frac{q}{\beta} \sim \frac{I[O]}{\gamma_1 [N_2] + \gamma_2 [O_2]}, \tag{6}$$

where q, β, I, and γ_1, γ_2 are the production term, the loss term, the solar ionizing flux, and the reaction rates, respectively.

The composition of the T/I system is mainly controlled by various production and loss mechanisms. The production of electrons is mainly due to the ionization of atomic oxygen through solar EUV, and the loss is mainly controlled by

N$_2$. The production of atomic oxygen ions depends not only on the atomic oxygen density, but also on the solar radiation. Ren et al. (2018) explained that the delay observed in the electron density depends on the production and loss processes as well as the [O]/[N$_2$] ratio. The major loss of ions in the F regions is given by the following reactions:

$$O^+ + N_2 \rightarrow NO^+ + N$$
$$O^+ + O_2 \rightarrow O_2^+ + O.$$
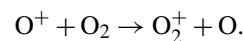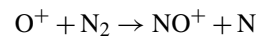
The rate coefficients γ_1 and γ_2 in Eq. (6) are given, e.g., by St.-Maurice and Torr (1978). These reaction rate coefficients are dependent on the effective temperature (T_f), which significantly affects the loss reaction and composition:

$$T_f = 0.63 \times T_i + 0.36 \times T_N. \tag{7}$$

Here T_i and T_N are ion temperature and the neutral temperature, respectively. For low values of $T_f < 1100$ K, the loss rate coefficients γ_1 and γ_2 decrease with increasing T_f, while for $T_f > 1100$ K, the loss rate γ_1 increases as a result of the electron density decrease with increasing F10.7 index. The nonlinear relation between the loss rate coefficients and T_f is shown by Su et al. (1999).

Figure 12 shows the variations of the [O]/[N$_2$] ratio for different diffusion conditions at geographical latitude/longitude 40° N, 18° E at an altitude of about 260 km (pressure level 12). For the reference run, the delay is about 2–3 d, since the peak response is observed at day 16. The [O]/[N$_2$] ratio strongly decreases with increasing eddy diffusion, and the delay is also shifted to 1 d. Thus, the variation in eddy diffusion strongly affects the [O]/[N$_2$] ratio, which in turn affects the delay mechanism.

Figure 13 shows the effect of eddy diffusion on the atomic oxygen ionization (a) and loss rates (c) through molecular nitrogen at 40° N, 18° E, and the difference between the reference run and other diffusion cases is shown in Fig. 13b and d. The reference case $K_T \times 1.0$ and the $K_T \times 0.75$ and $K_T \times 1.25$ runs are represented by blue, black, and red curves, respectively. The maximum ionization occurs at pressure level 9–10 (162–187 km) (Fig. 13a). Figure 13b shows a decrease of ionization rates with enhanced eddy diffusion, whereas they are increased for reduced eddy diffusion. The production term in Eq. (6) depends strongly on the ionization rates and the atomic oxygen density. Therefore, increased eddy diffusion decreases ionization and atomic oxygen density. Figure 13d shows that the loss rates are reduced by about 0.5 % in the F region in the case of enhanced eddy diffusion. Su et al. (1999) discussed the dependence of the loss rates on temperature. They suggested that the loss rate coefficient decreases with increasing T_f. Enhanced eddy diffusion leads to an increase in molecular components while reducing atomic oxygen.

Consequently, enhanced N_2 increases the overall loss term in Eq. (6) and reduces the electron density, resulting in a reduced delay in TEC. Based on the model simulations, we conclude that eddy diffusion is one of the major factors responsible for the changes in thermospheric composition via general circulation and significantly affects the ionospheric delay. Although the current investigation suggests that a small change in loss rates can affect the delay for several hours, further numerical modeling using real observations and varying atmospheric conditions is needed to understand the physical processes.

4 Summary

Using a 1-D model, Jakowski et al. (1991) first reported that the delayed density variation concerning solar EUV variations is probably due to the slow diffusion of atomic oxygen. Based on their hypothesis, the ionospheric delay in TEC, simulated by the CTIPe model, was investigated. Using the F10.7 index, the ionospheric delay at the solar rotation period is well reproduced and amounts to about 1 d (Jacobi et al., 2016; Schmölter et al., 2018). The thermosphere–ionosphere coupling plays an important role in the delay mechanism, and this was reported in several studies, but it was barely investigated. Therefore, this is the first time we investigated the impact of eddy diffusion on the ionospheric delay. To investigate the physical mechanism of ionospheric delay at the solar rotation period, we performed various experiments using CTIPe model. From the mechanistic studies using CTIPe, results show that eddy diffusion is an important factor that strongly influences the delay introduced in TEC based on the solar activity conditions. In the case of reduced eddy diffusion to 75 % of the original value, the delay is slightly longer (about 25 h), while in the case of increased transport, the de-

lay is reduced to 20 h. An increase in eddy diffusion leads to faster transport processes and an increased loss rate, resulting in a reduction of the ionospheric time delay.

At low latitudes, the influence of solar activity is stronger, as EUV radiation drives ionization processes that lead to compositional changes. Therefore, the combined effect of eddy diffusion and solar activity shows more delay in the low-latitude and midlatitude region.

Our results suggest that eddy diffusion plays a crucial role in the ionospheric delay. Therefore, further numerical modeling and observational results are required to better understand the role of lower atmospheric forcings and thermosphere–ionosphere coupling.

For this study, constant atmospheric conditions have been used to understand the role of solar flux and eddy diffusion in the ionospheric delay. In future, further investigation is required to explore the physical processes using actual observations. It would also be interesting to investigate the combined effect of solar variations, geomagnetic variations, and lower atmospheric forcings.

Author contributions. RV together with CJ and MC performed the CTIPe model simulations. RV drafted the first version of the manuscript. All authors discussed the results and contributed to the final version of the manuscript.

References

Afraimovich, E. L., Astafyeva, E. I., Oinats, A. V., Yasukevich, Y. V., and Zhivetiev, I. V.: Global electron content: a new conception to track solar activity, Ann. Geophys., 26, 335–344, https://doi.org/10.5194/angeo-26-335-2008, 2008.

Anderson, P. C. and Hawkins, J. M.: Topside ionospheric response to solar EUV variability, J. Geophys. Res.-Space, 121, 1518–1529, https://doi.org/10.1002/2015ja021202, 2016.

Brasseur, G. P. and Solomon, S.: Aeronomy of the middle atmosphere: Chemistry and physics of the stratosphere and mesosphere, Vol. 32, 3rd Edn., 646 pp., Springer, Dordrecht, the Netherlands, 2005.

Chandra, S. and Sinha, A. K.: The role of eddy turbulence in the development of self-consistent models of the lower and upper thermospheres, J. Geophys. Res., 79, 1916–1922, https://doi.org/10.1029/ja079i013p01916, 1974.

Codrescu, M. V., Fuller-Rowell, T. J., Munteanu, V., Minter, C. F., and Millward, G. H.: Validation of the Coupled Thermosphere Ionosphere Plasmasphere Electrodynamics model: CTIPE-Mass Spectrometer Incoherent Scatter temperature comparison, Space Weather, 6, S09005, https://doi.org/10.1029/2007sw000364, 2008.

Codrescu, M. V., Negrea, C., Fedrizzi, M., Fuller-Rowell, T. J., Dobin, A., Jakowsky, N., Khalsa, H., Matsuo, T., and Maruyama, N.: A real-time run of the Coupled Thermosphere Ionosphere Plasmasphere Electrodynamics (CTIPe) model, Space Weather, 10, S02001, https://doi.org/10.1029/2011sw000736, 2012.

Colegrove, F. D., Hanson, W. B., and Johnson, F. S.: Eddy diffusion and oxygen transport in the lower thermosphere, J. Geophys. Res., 70, 4931–4941, https://doi.org/10.1029/jz070i019p04931, 1965.

Danilov, A. D. and Konstantinova, A. V.: Reduction of the atomic oxygen content in the upper atmosphere, Geomagn. Aeronomy, 54, 224–229, https://doi.org/10.1134/s0016793214020066, 2014.

Fuller-Rowell, T. J.: A two-dimensional, high-resolution, nested-grid model of the thermosphere: 1. Neutral response to an electric field "spike", J. Geophys. Res., 89, 2971, https://doi.org/10.1029/ja089i05p02971, 1984.

Fuller-Rowell, T. J. and Rees, D.: A Three-Dimensional Time-Dependent Global Model of the Thermosphere, J. Atmos. Sci., 37, 2545–2567, https://doi.org/10.1175/1520-0469(1980)037<2545:atdtdg>2.0.co;2, 1980.

Fuller-Rowell, T. J. and Rees, D.: Derivation of a conservation equation for mean molecular weight for a two-constituent gas within a three-dimensional, time-dependent model of the thermosphere, Planet. Space Sci., 31, 1209–1222, https://doi.org/10.1016/0032-0633(83)90112-5, 1983.

Fuller-Rowell, T. J. and Rees, D.: Turbulent diffusion variability and implications for the upper thermosphere, Adv. Space Res., 12, 45–56, https://doi.org/10.1016/0273-1177(92)90443-2, 1992.

Fuller-Rowell, T. J., Rees, D., Quegan, S., Moffett, R., and Bailey, G.: Interactions between neutral thermospheric composition and the polar ionosphere using a coupled ionosphere-thermosphere model, J. Geophys. Res., 92, 7744, https://doi.org/10.1029/ja092ia07p07744, 1987.

Jacobi, C., Jakowski, N., Schmidtke, G., and Woods, T. N.: Delayed response of the global total electron content to solar EUV variations, Adv. Radio Sci., 14, 175–180, https://doi.org/10.5194/ars-14-175-2016, 2016.

Jakowski, N., Fichtelmann, B., and Jungstand, A.: Solar activity control of ionospheric and thermospheric processes, J. Atmos. Terr. Phys., 53, 1125–1130, https://doi.org/10.1016/0021-9169(91)90061-b, 1991.

Jones, M., Forbes, J. M., and Hagan, M. E.: Tidal-induced net transport effects on the oxygen distribution in the thermosphere, Geophys. Res. Lett., 41, 5272–5279, https://doi.org/10.1002/2014gl060698, 2014a.

Jones, M., Forbes, J. M., Hagan, M. E., and Maute, A.: Impacts of vertically propagating tides on the mean state of the ionosphere-thermosphere system, J. Geophys. Res.-Space, 119, 2197–2213, https://doi.org/10.1002/2013ja019744, 2014b.

Jones, M., Emmert, J. T., Drob, D. P., Picone, J. M., and Meier, R. R.: Origins of the Thermosphere-Ionosphere Semiannual Oscillation: Reformulating the "Thermospheric Spoon" Mechanism, J. Geophys. Res.-Space, 123, 931–954, https://doi.org/10.1002/2017ja024861, 2018.

Keneshea, T. J. and Zimmerman, S. P.: The Effect of Mixing Upon Atomic and Molecular Oxygen in the 70–170 km Region of the Atmosphere, J. Atmos. Sci., 27, 831–840, https://doi.org/10.1175/1520-0469(1970)027<0831:teomua>2.0.co;2, 1970.

Kirchhoff, V. W. J. H. and Clemesha, B. R.: Eddy diffusion coefficients in the lower thermosphere, J. Geophys. Res., 88, 5765, https://doi.org/10.1029/ja088ia07p05765, 1983.

Lee, C.-K., Han, S.-C., Bilitza, D., and Seo, K.-W.: Global characteristics of the correlation and time lag between solar and ionospheric parameters in the 27-day period, J. Atmos. Sol.-Terr. Phys., 77, 219–224, https://doi.org/10.1016/j.jastp.2012.01.010, 2012.

Li, F., Liu, A. Z., and Swenson, G. R.: Characteristics of instabilities in the mesopause region over Maui, Hawaii, J. Geophys. Res., 110, D09S12, https://doi.org/10.1029/2004jd005097, 2005.

Liu, L., Wan, W., Ning, B., Pirog, O. M., and Kurkin, V. I.: Solar activity variations of the ionospheric peak electron density, J. Geophys. Res., 111, A08304, https://doi.org/10.1029/2006ja011598, 2006.

Meraner, K. and Schmidt, H.: Transport of nitrogen oxides through the winter mesopause in HAMMONIA, J. Geophys. Res.-Atmos., 121, 2556–2570, https://doi.org/10.1002/2015jd024136, 2016.

Millward, G., Moffett, R., Quegan, S., and Fuller-Rowell, T.: A coupled thermosphere-ionosphere-plasmasphere model (CTIP), STEP handbook on ionospheric models, 239–279, 1996.

Pilinski, M. D. and Crowley, G.: Seasonal variability in global eddy diffusion and the effect on neutral density, J. Geophys. Res.-Space, 120, 3097–3117, https://doi.org/10.1002/2015ja021084, 2015.

Qian, L., Solomon, S. C., and Kane, T. J.: Seasonal variation of thermospheric density and composition, J. Geophys. Res.-Space, 114, A01312, https://doi.org/10.1029/2008ja013643, 2009.

Qian, L., Burns, A. G., Solomon, S. C., and Wang, W.: Annual/semiannual variation of the ionosphere, Geophys. Res. Lett., 40, 1928–1933, https://doi.org/10.1002/grl.50448, 2013.

Quegan, S., Bailey, G., Moffett, R., Heelis, R., Fuller-Rowell, T., Rees, D., and Spiro, R.: A theoretical study of the distribution of ionization in the high-latitude ionosphere and the plasmasphere: first results on the mid-latitude trough and the light-ion trough, J. Atmos. Terr. Phys., 44, 619–640, https://doi.org/10.1016/0021-9169(82)90073-3, 1982.

Rees, D. and Fuller-Rowell, T.: Understanding the transport of atomic oxygen within the thermosphere, using a numerical global thermospheric model, Planet. Space Sci., 36, 935–948, https://doi.org/10.1016/0032-0633(88)90101-8, 1988.

Ren, D., Lei, J., Wang, W., Burns, A., Luan, X., and Dou, X.: Does the Peak Response of the Ionospheric F2 Region Plasma Lag the Peak of 27-Day Solar Flux Variation by Multiple Days?, J. Geophys. Res.-Space, 123, 7906–7916, https://doi.org/10.1029/2018ja025835, 2018.

Ren, D., Lei, J., Wang, W., Burns, A., Luan, X., and Dou, X.: A Simulation Study on the Time Delay of Daytime Thermospheric Temperature Response to the 27-Day Solar EUV Flux Variation, J. Geophys. Res.-Space, 124, 9184–9193, https://doi.org/10.1029/2019ja027000, 2019.

Ren, D., Lei, J., Wang, W., Burns, A., Luan, X., and Dou, X.: Different Peak Response Time of Daytime Thermospheric Neutral Species to the 27-Day Solar EUV Flux Variations, J. Geophys. Res.-Space, 125, e2020JA027840, https://doi.org/10.1029/2020ja027840, 2020.

Ren, D., Lei, J., Wang, W., Burns, A., and Luan, X.: Observations and simulations of the peak response time of thermospheric mass density to the 27-day solar EUV flux variation, J. Geophys. Res.-Space, 126, e2020JA028756, https://doi.org/10.1029/2020JA028756, 2021.

Richards, P. G., Fennelly, J. A., and Torr, D. G.: EUVAC: A solar EUV Flux Model for aeronomic calculations, J. Geophys. Res., 99, 8981, https://doi.org/10.1029/94ja00518, 1994.

Richmond, A. D., Ridley, E. C., and Roble, R. G.: A thermosphere/ionosphere general circulation model with coupled electrodynamics, Geophys. Res. Lett., 19, 601–604, https://doi.org/10.1029/92gl00401, 1992.

Rishbeth, H.: How the thermospheric circulation affects the ionospheric F2 layer, J. Atmos. Sol.-Terr.l Phys., 60, 1385–1402, https://doi.org/10.1016/s1364-6826(98)00062-5, 1998.

Rishbeth, H., Fuller-Rowell, T., and Rees, D.: Diffusive equilibrium and vertical motion in the thermosphere during a severe magnetic storm : A computational study, Planet. Space Sci., 35, 1157–1165, https://doi.org/10.1016/0032-0633(87)90022-5, 1987.

Sasi, M. N. and Vijayan, L.: Turbulence characteristics in the tropical mesosphere as obtained by MST radar at Gadanki (13.5° N, 79.2° E), Ann. Geophys., 19, 1019–1025, https://doi.org/10.5194/angeo-19-1019-2001, 2001.

Schmölter, E., Berdermann, J., Jakowski, N., Jacobi, C., and Vaishnav, R.: Delayed response of the ionosphere to solar EUV variability, Adv. Radio Sci., 16, 149–155, https://doi.org/10.5194/ars-16-149-2018, 2018.

Schmölter, E., Berdermann, J., Jakowski, N., and Jacobi, C.: Spatial and seasonal effects on the delayed ionospheric response to solar EUV changes, Ann. Geophys., 38, 149–162, https://doi.org/10.5194/angeo-38-149-2020, 2020.

Schmölter, E., Berdermann, J., and Codrescu, M.: The delayed ionospheric response to the 27-day solar rotation period analyzed with GOLD and IGS TEC data, J. Geophys. Res.-Space, 126, e2020JA028861, https://doi.org/10.1029/2020JA028861, 2021.

Shim, J. S., Kuznetsova, M., Rastätter, L., Hesse, M., Bilitza, D., Butala, M., Codrescu, M., Emery, B., Foster, B., Fuller-Rowell, T., Huba, J., Mannucci, A. J., Pi, X., Ridley, A., Scherliess, L., Schunk, R. W., Stephens, P., Thompson, D. C., Zhu, L., Anderson, D., Chau, J. L., Sojka, J. J., and Rideout, B.: CEDAR Electrodynamics Thermosphere Ionosphere (ETI) Challenge for systematic assessment of ionosphere/thermosphere models: NmF2, hmF2, and vertical drift using ground-based observations, Space Weather, 9, S12003, https://doi.org/10.1029/2011sw000727, 2011.

Shimazaki, T.: Effective eddy diffusion coefficient and atmospheric composition in the lower thermosphere, J. Atmos. Terr. Phys., 33, 1383–1401, https://doi.org/10.1016/0021-9169(71)90011-0, 1971.

Siskind, D. E., Drob, D. P., Dymond, K. F., and McCormack, J. P.: Simulations of the effects of vertical transport on the thermosphere and ionosphere using two coupled models, J. Geophys. Res.-Space, 119, 1172–1185, https://doi.org/10.1002/2013ja019116, 2014.

St.-Maurice, J. P. and Torr, D. G.: Nonthermal rate coefficients in the ionosphere: The reactions of O^+ with N_2, O_2, and NO, J. Geophys. Res., 83, 969–977, https://doi.org/10.1029/ja083ia03p00969, 1978.

Su, Y. Z., Bailey, G. J., and Fukao, S.: Altitude dependencies in the solar activity variations of the ionospheric electron density, J. Geophys. Res.-Space, 104, 14879–14891, https://doi.org/10.1029/1999ja900093, 1999.

Swenson, G., Yee, Y., Vargas, F., and Liu, A.: Vertical diffusion transport of atomic oxygen in the mesopause region consistent with chemical losses and continuity: Global mean and inter-annual variability, J. Atmos. Sol.-Terr. Phys., 178, 47–57, https://doi.org/10.1016/j.jastp.2018.05.014, 2018.

Swenson, G. R., Salinas, C. C. J. H., Vargas, F., Zhu, Y., Kaufmann, M., Jones, M., Drob, D. P., Liu, A., Yue, J., and Yee, J. H.: Determination of Global Mean Eddy Diffusive Transport in the Mesosphere and Lower Thermosphere From Atomic Oxygen and Carbon Dioxide Climatologies, J. Geophys. Res.-Atmos., 124, 13519–13533, https://doi.org/10.1029/2019jd031329, 2019.

Tapping, K. F.: Recent solar radio astronomy at centimeter wavelengths: The temporal variability of the 10.7-cm flux, J. Geophys. Res., 92, 829–838, https://doi.org/10.1029/jd092id01p00829, 1987.

Vaishnav, R., Jacobi, C., Berdermann, J., Schmölter, E., and Codrescu, M.: Ionospheric response to solar EUV variations: Preliminary results, Adv. Radio Sci., 16, 157–165, https://doi.org/10.5194/ars-16-157-2018, 2018.

Vaishnav, R., Jacobi, C., and Berdermann, J.: Long-term trends in the ionospheric response to solar extreme-ultraviolet variations, Ann. Geophys., 37, 1141–1159, https://doi.org/10.5194/angeo-37-1141-2019, 2019.

Vaishnav, R., Schmölter, E., Jacobi, C., Berdermann, J., and Codrescu, M.: Ionospheric response to solar extreme ultraviolet radiation variations: comparison based on CTIPe model simulations and satellite measurements, Ann. Geophys., 39, 341–355, https://doi.org/10.5194/angeo-39-341-2021, 2021.

Woods, T. N. and Rottman, G. J.: Solar ultraviolet variability over
time periods of aeronomic interest, in: Atmospheres in the Solar
System: Comparative Aeronomy, American Geophysical Union,
221–233, 2002.